Supporting Information

Park et al. 10.1073/pnas.1422649112

I. PPC Synthesis

S1. Materials and Synthesis of PPCs. All citrate-capped Au nanoparticles (AuNPs) were purchased from Ted Pella. The oligonucleotide sequences used in this work are summarized in Table S1. Oligonucleotides were either purchased from Integrated DNA Technologies or synthesized on an MM48 automated oligonucleotide synthesizer (BioAutomation), and all DNA synthesis reagents were obtained from Glen Research. After synthesis, oligonucleotides were purified by RP-HPLC (Agilent) on a Varian Microsorb C18 column (10 μm, 300 × 10 mm). The DNA conjugation with AuNPs was conducted following a literature procedure (1). Briefly, the alkyl thiolated DNA strands were treated with 100 mM DTT (Sigma-Aldrich) in PBS buffer solution for half an hour. The small molecules and salts were then removed by size-exclusion chromatography with a NAP5 column (Pharmacia Biotech). The collected DTT-treated DNA was directly mixed with the citrate-capped AuNPs at a ratio of one strand per square nanometer (this area is calculated from the surface area of the AuNPs) and incubated for 1 h. Then, stepwise additions of 5.0 M NaCl (with each aliquot raising the total NaCl concentration by ∼0.1 M) were made to the solution over 1-h intervals. Once a final buffer concentration of 0.5 M NaCl was reached, the solution was further incubated overnight to allow for maximum DNA loading. The resulting DNA-modified AuNPs were then purified with multiple (up to eight) rounds of centrifugation (2,000 relative centrifugal force, 10 min) using tubes fitted with 100-kDa cutoff membrane concentrators (Millipore). Each round was followed by removal of the filtrated solution and addition of more Nanopure water (18.2 MΩ). After the final centrifugation cycle the purified DNA-modified AuNPs were resuspended in water for future use.

To form BCC superlattices, two different sets of AuNPs were functionalized with different linkers (type A and B for 9.0- and 20-nm samples, PPC2 and PPC3; type C and D for 5.6-nm sample, PPC1) that presented complementary sticky ends ($^{5'}$TTCCTT$^{3'}$ and $^{5'}$AAGGAA$^{3'}$ for 20- and 9.0-nm samples; $^{5'}$TTTCCTT$^{3'}$ and $^{5'}$AAGGAAA$^{3'}$ for 5.6-nm sample) for each size of AuNPs. In these systems, the DNA linkers were first hybridized to the appropriate particles by combining the linkers and the DNA-modified AuNPs, heating the solution to 50 °C for ∼30 min, and then slowly cooling to room temperature. This was done to ensure that the maximum number of DNA linkers was hybridized to each particle. These two nanoparticle solutions containing complementary linkers were then combined in a 1:1 ratio. Following precipitation, the AuNP aggregates were slowly annealed according to the reported procedure to form rhombic dodecahedron single crystals (2). Generally, the samples were heated to 50 °C and then slowly cooled to room temperature on a PCR machine (Life Technologies) at a cooling rate of 0.1 °C/10 min. After annealing, the aggregates were then transferred to quartz capillaries for small angle X-ray scattering (SAXS) measurements and subsequent silica embedding.

All superlattices used for optical measurement and SEM imaging were first embedded in amorphous silica using established protocols [experimental information is discussed in more detail in previous work (3)]. Briefly, the superlattices were first incubated with excess *N*-trimethoxysilylpropyl-*N*,*N*,*N*-trimethlyammonium chloride (Gelest) for ∼10 min, followed by the addition of triethoxysilane (Sigma-Aldrich). This mixture was stirred vigorously for 4 d at room temperature, after which the resulting precipitate was purified by three rounds of centrifugation in water (21,000 relative centrifugal force, 10 min). This precipitate was then transferred onto an ITO-coated glass slide for optical measurements and SEM imaging. SEM imaging was conducted with a Hitachi SU8030 instrument.

S2. SAXS Characterization of PPCs. SAXS characterization (Fig. S1) was carried out at the DuPont–Northwestern–Dow Collaborative Access Team beamline of Argonne National Laboratory's Advanced Photon Source. X-rays of wavelength 1.24 Å (10 keV) were used, and the system was calibrated using silver behenate as a standard. Two sets of slits were used to define and collimate the X-ray beam; parasitic scattering was removed via a pinhole. Typical exposure times varied between 0.1 and 0.5 s, depending upon the sample. The scattered X-rays were collected with a CCD area detector and 1D scattering data were obtained from radial averaging of the 2D data to obtain plots of scattering intensity as a function of the scattering vector q, $q = 4\pi \sin\theta/\lambda$, where θ is one-half of the scattering angle and λ is the wavelength of the X-rays used. Scattering from the buffer and DNA was negligible compared with scattering from the AuNPs. Structure factors [S(q)] were calculated by dividing the raw data by a scan of the sample's form factor F(q), obtained by collecting SAXS data of nonaggregated particles (AuNPs with no linker added).

For the assembly parameters presented in the previous section, all relevant interparticle distances and lattice parameters were calculated using the SAXS data. In a superlattice with BCC structure the distance between nanoparticle nearest neighbors within a particle superlattice can be determined by $d_{NP} = (1/10)(C/q_0)$, where d_{NP} is the distance in nanometers between two NP nearest neighbors, q_0 is the position of the initial scattering peak in 1/angstrom, and C is a constant that correlates the distance between two nanoparticle nearest neighbors and the distance between the [*hkl*] planes associated with the first scattering peak. The value of C for BCC superlattices is equal to $\sqrt{6}\pi$. Interparticle distances and lattice parameters of superlattices assembled with different AuNPs were calculated from SAXS patterns and are listed in Table S2.

II. Theoretical and Experimental Analysis of PPC Optical Response

S3. Geometric Optics Approximation of the Backscattering by a Rhombic Dodecahedron Structure. The backscattering of a plane wave by a dielectric rhombic dodecahedron structure (Fig. 1*A*) can be approximated with a reasonably small error by geometric optics when its size parameter, $\pi L n/\lambda$, is greater than ∼20 (4, 5), where L and n are the long axis (distance between leftmost and rightmost vertices in Fig. 1*A*) and refractive index of the structure, respectively, and λ is the wavelength of the interacting light. In Fig. 1*B*, the vertical cross-section (a hexagon) of the gray area in the top right inset of Fig. 1*A* is shown. The majority of light is backscattered through this scattering channel in the geometric optics approximation. In Fig. S2 the backscattering through the parallel center facets and the slanted side facets are extensively described in the case of dielectric structures. First, the backscattering from the parallel center facets (red arrows) generates the Fabry–Perot modes in the geometric optics limit. FPMs are resonant modes owing to the repeated trips between the top and bottom facets. Second, the backscattering through the slanted side facets (blue arrows) can be analyzed as follows: A light ray incident on the first facet **A** with incident angle θ_{1i} (60°) reflects from facet **C** and can refract through facet **B** if the refractive index is below that of the total internal reflection limit and

$\tan^{-1}(1/3\sqrt{3}) < \theta_{1t} < \tan^{-1}(5/3\sqrt{3})$. In this case, $\theta_{1i} = \theta_{3t}$ (60°) because $\theta_{2i} = \theta_{2r}$. When the structure exhibits a complex refractive index such as that of our PPCs it requires a more sophisticated version of a geometric optics analysis (6, 7) to analyze the scattering through the side slanted facets (blue arrows) because the angles of refraction and transmission deviate from those predicted by conventional Fresnel's law to a certain degree. Because this scattering channel is not the focus of this work we do not discuss it further here. Owing to symmetry, the ray incident on facet **B** experiences the same scattering process as the ray incident on the other side (**A**).

S4. Optical Setup for Backscattering Signal Detection and Imaging. Microspectrophotometry was performed to probe the FPMs by detecting the backscattering signal from PPCs (Fig. S3). Here, a Zeiss Axio Observer.Z1m microscope was used. A spectrometer (Acton series; Princeton Instruments) and CCD (PyLoN) were used for spectral detection. The light source was a xenon lamp (XBO 75) that has a broad-band spectrum of 300–1,100 nm. The sizes of the field-stop and aperture were minimized in the bright field (BF) reflection mode to minimize the angle of light injection. A 50× objective (N.A. 0.8) was used for light collection to avoid interference between FPMs and signal from the side slanted facets. The light was extracted from the bright spot at the center of PPCs to detect only FPMs, not the signal from the slanted facet. The spectrometer grating setup was 50 g/mm. To normalize the PPC backscattering spectrum by the lamp profile the lamp spectrum was separately collected by BF transmission mode (not shown in Fig. S3). The normalized intensity of the backscattering spectra in Fig. 2 is $R_{raw} = I_{RL}^{PPC}/I_{TR}^{XBO}$, where I_{RL}^{PPC} is the signal intensity from the center of the PPCs and I_{TR}^{XBO} is the XBO intensity; 50× and 100× objectives were used for imaging.

S5. FDTD Calculations. The FDTD simulations were performed with a commercial package (Lumerical FDTD Solutions v.8.7.0). The dielectric functions of gold and silver were adopted from the experimental data of ref. 8, and the refractive index of the silica host medium in the PPCs was assumed to be 1.43 in this work. Three types of FDTD calculations have been carried out as follows (Fig. S4).

1. $FDTD_{EMT\text{-}RD}$: Proof of FPMs and reproduction of BF image of PPCs. To prove the Fabry–Perot nature of the backscattering signal from the center of the PPCs and to reproduce the microscope image of PPCs, a FDTD simulation was performed with rhombic dodecahedron geometry. The BCC gold nanoparticle superlattice was approximated by effective medium theory (see section S6 below) owing to computational limitations. To take into account the smooth edges of PPCs, the radius of curvature at each edge was defined as 10% of L. A dielectric substrate (refractive index 1.44) was added to include the effect of the glass slide. Mesh step size was 10 nm. The perfectly matched layer (PML) boundary condition was used to absorb the electromagnetic fields at the simulation boundary. Two polarization states were used: parallel and perpendicular to the long axis of the PPCs. The Gaussian illumination was performed with an N.A. value of 0.2. After the scattering calculation, the backscattered near-field was post-processed by far-field projection with N.A. 0.8 to simulate the effect of the 50× objective lens used in the experiment. Out of 100 × 100 pixels of the processed images, 10 × 10 pixels at the center of the PPCs were selected and averaged to generate the backscattering spectrum (red lines; Fig. S5). Owing to the large N.A. value, spectra from the center of the far-field projected images mainly contain the components backscattered from the parallel center facets. Below N.A. 0.5, a significant interference between the two scattering channels (the center and slanted facets) is observed (not shown in Fig. S5).

In Fig. S5*A* we observe good agreement between results from the above $FDTD_{EMT\text{-}RD}$ setup (red solid and dashed lines) and the 2D infinite EMT slab model (blue solid line) for the 11% volume fraction (*FF*) and L = 4.0 μm sample. (See section S6 and Fig. S6 for the EMT approximation and 2D infinite slab model.) Because the 2D infinite EMT slab model exhibits only Fabry–Perot modes, this is proof of the Fabry–Perot-like nature of the backscattering from the center parallel facets of PPCs. Their mode positions (dips in backscattering spectra) deviate beyond 800 nm. This is probably because of the decreased size parameter, $\pi L\, n_{eff}(\lambda)/\lambda$, owing to a low refractive index (Fig. S6*A*) and a smaller relative ratio of structure size and wavelength at larger wavelengths. Although the PPC still maintains the Fabry–Perot nature of backscattering, the optical path that light experiences becomes slightly larger than the physical thickness of the PPC as the size parameter decreases. The images in the top inset of Fig. S5*A* are the far-field projected images from five different spectral positions (square marks on red solid line). The intensity of the bright spot at the center decreases at the dips and increases at the peaks as in Fabry–Perot resonators. As expected, there is not a significant difference between the two polarizations (red solid and dashed lines) owing to the Fabry–Perot nature.

In Fig. S5 *B–E* the same data for the PPCs of L = 2.0–0.5 μm are shown. As L decreases, the spectral positions deviate significantly between the $FDTD_{EMT\text{-}RD}$ model (red solid lines) and 2D infinite slab model (blue solid lines). As mentioned above, this is due to the increase in the optical path length. Below L = 1.0 μm the spectral shape itself is very different from those of larger sizes, indicating breakdown of the geometric optics approximation. To compensate for the increased optical path length of PPCs for L = 2.0–0.5 μm, the thickness of the slab in the 2D infinite slab model was increased by 8–18% depending on L. The results with this increased thickness (magenta solid lines) match with the results from the $FDTD_{EMT\text{-}RD}$ model within the visible range.

2. $FDTD_{BCC\text{-}slab}$: Backscattering spectra from 2D infinite BCC slab. The reflectance spectra of 2D infinite BCC slabs of gold nanoparticles shown in Fig. 2 were calculated by constructing the BCC structures in the FDTD spatial domain. The diameter and lattice constant were 5.6 and 27.2 nm for PPC1, 9.0 and 32.2 nm for PPC2, and 20.0 nm and 44.0 nm for PPC3. A dielectric substrate was added to simulate the effects of the glass slide (PPC2–3; refractive index 1.44) and a silicon substrate (PPC1; ref. 9). Symmetric boundary conditions were applied in the in-plane (x–y) directions. A PML boundary condition was used in the light propagation direction (out-of-plane, z). The mesh step size was 5 nm. The crystal structures were oriented so that the ΓN direction is parallel to the light propagation direction as in the experimental samples. Fig. 2 *B*, *D*, and *F* show good agreement between $FDTD_{BCC\text{-}slab}$ results and the EMT-based results (see section S6 below). For PPC3 the FPMs are heavily suppressed below λ ~650 nm in the $FDTD_{BCC\text{-}slab}$ result, whereas they are suppressed below λ ~600 nm in the EMT-based spectrum. This is probably due to near-field coupling among the gold nanoparticles in $FDTD_{BCC\text{-}slab}$. In Fig. 4, silver layers were added on the top and bottom surfaces of the slabs to enhance the Q factor.

3. $FDTD_{BCC\text{-}PhC}$: Photonic crystal analysis and dispersion diagrams of PPCs. To generate the spectral densities in the ΓN direction of the PPCs (Fig. 3 *A–C* and Fig. S7 *A–F*), Bloch boundary conditions were used in all three directions (x, y, and z). The unit cell was excited with randomly distributed multiple dipole sources. The electric fields at four different points near a gold nanoparticle in the unit cell were recorded and Fourier-transformed to produce the photonic density of states. The distance between the gold nanoparticle surface and the data collection points was about half of the nanoparticle radius to extract enough signal from the plasmonic modes.

S6. Effective Medium Theory Approximation and 2D Infinite Slab Model. In this work, we adopt EMT (10, 11) to approximate the refractive indices of PPCs to reduce the size of the

$FDTD_{EMT\text{-}RD}$ simulation and to validate $FDTD_{BCC\text{-}slab}$ and $FDTD_{BCC\text{-}PhC}$. EMT can accurately describe the effective refractive indices of PPCs when the interparticle near-field coupling is negligible and the resonance of individual particles is mainly dominated by the dipolar resonance. These conditions are typically met when the volume fraction of the inclusion is less than 20% and the diameter of the inclusion is small (12). PPC1–3 satisfy these criteria. EMT describes the dielectric constants of the PCCs by the Maxwell–Garnett equation, $\varepsilon_{eff}-\varepsilon_{host}/\varepsilon_{eff}+2\varepsilon_{host}=FF(\varepsilon_{inc}-\varepsilon_{host}/\varepsilon_{inc}+2\varepsilon_{host})$, where FF is the inclusion (gold) volume fraction and ε_{eff}, ε_{inc}, and ε_{host} are dielectric constants of the effective superlattice medium, inclusion, and silica host medium, respectively. Here, $FF=2(4/3)\pi r^3/a^3$, where r is the radius of gold nanoparticles and a is the lattice constant of BCC lattices. Fig. S6 *A* and *B* shows the real and imaginary parts of the effective refractive indices with several different gold volume fractions. The peak positions of the real parts are close to the surface plasmon resonance frequency, and they are red-shifted at higher gold volume fractions. Overall, the real and imaginary parts increase at higher volume fractions owing to the increase in polarizability of the effective medium.

The reflectance from a 2D infinite slab of EMT medium (the rightmost scheme in Fig. S4) is calculated by taking the absolute square of the reflection coefficient of a single slab (13, 14), $R=\rho_L+\rho_R e^{2ikn_{eff}l}/1+\rho_L\rho_R e^{2ikn_{eff}l}$, where $\rho_L=n_0-n_{eff}/n_0+n_{eff}$ and $\rho_R=n_{eff}-n_t/n_{eff}+n_t$, and n_0, n_t and $n_{eff}=\sqrt{\varepsilon_{eff}}$ are the refractive indices of the surrounding media (n_0: light reflection side, n_t: light transmission side) and of a PPC. To assign the FPM mode number (N) for Fig. 3 *A–C*, the resonant condition of a Fabry–Perot cavity, $\omega_N=N(c/\mathrm{Re}[n_{eff}])(\pi/l)=(c/\mathrm{Re}[n_{eff}])k_N$, was used (13, 14).

S7. Quantification of Mode Splitting Based on $FDTD_{BCC\text{-}PhC}$ and EMT. The mode splitting values presented in Fig. 3 *A–D* are generated by fitting dispersion information based on the $FDTD_{BCC\text{-}PhC}$ and EMT models to a Lorentzian line shape (see chaps. 4 and 5 in ref. 15).

First, in Fig. S7 *A–C* (the same dispersion diagrams as Fig. 3 *A–C* with a larger range), the upper and lower polariton branches for PPC1–3 (peak positions of photonic spectral density) generated by $FDTD_{BCC\text{-}PhC}$ with the experimentally measured dielectric constant (8) are fitted with a Lorentzian line shape: $\varepsilon(\omega)=\varepsilon_b+f/\omega_0^2-\omega^2-i\omega\gamma$, where ε_b (background dielectric constant), γ (damping factor), ω_0 (eigen-frequency of the polar materials), and f (oscillator strength) are fitting parameters. Based on ε_b and ω_0, light lines and plasmon resonant frequencies are indicated, allowing one to find the resonant coupling points in the dispersion diagrams. The energy gaps between the upper and lower branches at the resonant coupling points are the mode splitting values, $\hbar\Omega_R$ (red arrows; Fig. 3*D*, circles). In Fig. S7*C*, a very weak upper branch is observed for PPC3 owing to strong absorption by the gold interband transition, and the mode splitting is not determined because the upper branch is not experimentally observed (Fig. 2*F*). To remove the effect of the gold interband transition in the dispersion diagrams, the same $FDTD_{BCC\text{-}PhC}$ for PPC1–3 were performed with a gold dielectric constant generated by the Drude model (Fig. S7 *D–F*; Fig. 3*D*, squares) (16): $\varepsilon_D(\omega)=\varepsilon_\infty-(\omega_D^2/\omega^2+i\gamma_D\omega)$, where ($\varepsilon_\infty$, ω_D, γ_D) = (11.4577, 9.4027 eV, and 0.08314 eV), as shown in Fig. S7*G*. In Fig. S7*F* the upper branch is clearly observable, and therefore the mode splitting is quantified (red arrow; $\hbar\Omega_R$~30% of $\hbar\omega_0$).

Second, the EMT approximation with the above Drude model was used to generate the dispersion diagrams for PPCs with 1–12% gold volume fractions and the dispersion information was fitted with the Lorentzian line shape above (Fig. S7*H*; PPC with 10% gold volume fraction). Based on the fitting results (Fig. S7*I*), the mode splitting data were generated (red arrow in Fig. S7*H*; Fig. S7*J* and Fig. 3*D*).

S8. Calculations of *Q* Factor. To analyze the performance of silver-coated PPCs as plasmonic microcavities we estimate their Q factor by FDTD simulations. Because we focus on the cavity modes that hybridize FPMs and localized surface plasmons (see the main text, Fig. 4), we use $FDTD_{BCC\text{-}slab}$, which exhibits only FPMs. Silver layers (10–30 nm) are added to the top and bottom of the BCC slab structures, and the thicknesses of PPC1–3 slabs are ~1.3 μm.

For Q factor evaluation, the cavity internal electric fields in the time domain (Fig. S8*A*) were Fourier-transformed to generate electric fields in the spectral domain (Fig. S8*B*). Then, Q factors were assigned to each resonant position (Fig. 4) based on $Q=\omega/\Delta\omega$. The Q factors of PPC1–3 can be decomposed into two components: $Q^{-1}=Q_{SP}^{-1}+Q_{FPMs}^{-1}$, where Q_{SP}^{-1} is the ohmic loss by the plasmonic (gold) nanoparticles and Q_{FPMs}^{-1} is the loss caused by radiation and silver absorption at the cavity facets. Owing to large ohmic loss in the gold nanoparticles, the PCCs are Q_{SP}-limited with small Q factors close to the LSPR frequency (Fig. 4). These Q values are relatively small compared with conventional dielectric cavities. Well removed from the LSPR frequency, the Q factor increases as the gold ohmic loss decreases. From PPC3 to PPC1 the Q factor increases gradually (Fig. 4) because the gold volume fraction and the corresponding ohmic loss decrease.

III. Sample Postprocessing for Enhancing *Q* Factor of PPCs

S9. PPC Silver Coating. A simple PPC silver layer coating method was developed to improve the Q factor of the FPMs (Fig. S9). First, a batch of PPCs was deposited on a glass slide as in Fig. S9*A* and a PPC of desired size was chosen. Before the silver coating process, the optical performance of the PPC was confirmed with the backscattering measurement. Then, a 30-nm silver layer was deposited on the PPC by e-beam deposition as in Fig. S9*B*. To access the uncoated bottom side of the PPC, a sticky 30-μm-diameter polydimethylsiloxane (PDMS) pillar was used to lift the PPC from the glass slide. The PDMS pillar was made by molding the elastomer from a master with negative hole features. These features were fabricated by photolithography followed by deep reactive-ion etching. The bottom side of the PPC was exposed by pressing the PDMS pillar against the PPC and attaching the PPC to its surface as in Fig. S9*C*. Finally, another 30-nm silver layer was deposited on the uncoated side as in Fig. S9*D*. Fig. S9*E* shows the optical microscope images of a representative PPC on a PDMS pillar after the steps pictured in Fig. S9 *C*, *Top* and *D*, *Bottom*. The PPC top facet in the top image exhibits redder color that is consistent with the corresponding spectrum (black solid line) in Fig. S10*A*.

S10. Effect of Silver Coating on PPC Backscattering Spectra. Following silver layer coating (section S9), the backscattering spectrum is measured before and after the top layer is coated (Fig. S10*A*). Owing to enhanced facet reflection by the silver layer, the overall backscattering intensity increases, and very slight line sharpening is observed from the top-uncoated to the top-coated PPC3 (from black to red solid line). The line sharpening is slight owing to collection and illumination with a lens with N.A. 0.8 and surface roughness. Near-field profiles within this silver-coated PPC3 generated by $FDTD_{EMT\text{-}RD}$ (Fig. S10*B*) clearly reveal well-defined FPMs.

1. Macfarlane RJ, et al. (2011) Nanoparticle superlattice engineering with DNA. *Science* 334(6053):204–208.
2. Auyeung E, et al. (2014) DNA-mediated nanoparticle crystallization into Wulff polyhedra. *Nature* 505(7481):73–77.
3. Auyeung E, Macfarlane RJ, Choi CHJ, Cutler JI, Mirkin CA (2012) Transitioning DNA-engineered nanoparticle superlattices from solution to the solid state. *Adv Mater* 24(38):5181–5186.
4. Borovoi A, Konoshonkin A, Kustova N, Okamoto H (2012) Backscattering Mueller matrix for quasi-horizontally oriented ice plates of cirrus clouds: Application to CALIPSO signals. *Opt Express* 20(27):28222–28233.
5. Bi L, Yang P, Kattawar GW, Hu YX, Baum BA (2011) Scattering and absorption of light by ice particles: Solution by a new physical-geometric optics hybrid method. *J Quant Spectrosc Ra* 112(9):1492–1508.
6. Yang P, Liou KN (2009) An "exact" geometric-optics approach for computing the optical properties of large absorbing particles. *J Quant Spectrosc Ra* 110(13): 1162–1177.
7. Yang P, Liou KN (2009) Effective refractive index for determining ray propagation in an absorbing dielectric particle. *J Quant Spectrosc Ra* 110(4-5):300–306.
8. Johnson PB, Christy RW (1972) Optical constants of noble metals. *Phys Rev B* 6(12): 4370–4379.
9. Palik ED, Ghosh G (1998) *Handbook of Optical Constants of Solids* (Academic, San Diego).
10. Bergman DJ (1978) The dielectric constant of a composite material—A problem in classical physics. *Phys Rep* 43(9):378–407.
11. Ruppin R (2000) Evaluation of extended Maxwell-Garnett theories. *Opt Commun* 182(4–6):273–279.
12. Ross MB, Blaber MG, Schatz GC (2014) Using nanoscale and mesoscale anisotropy to engineer the optical response of three-dimensional plasmonic metamaterials. *Nat Commun* 5:4090.
13. Born M, Wolf E (1980) *Principles of Optics: Electromagnetic Theory of Propagation, Interference and Diffraction of Light* (Pergamon, Oxford), 6th Ed, p xxvii.
14. Fowles GR (1975) *Introduction to Modern Optics* (Holt, Rinehart and Winston, New York), 2nd Ed, p viii.
15. Klingshirn CF (2007) *Semiconductor Optics* (Springer, Berlin), 3rd Ed, p xxvii.
16. Chang SH, Gray S, Schatz G (2005) Surface plasmon generation and light transmission by isolated nanoholes and arrays of nanoholes in thin metal films. *Opt Express* 13(8): 3150–3165.

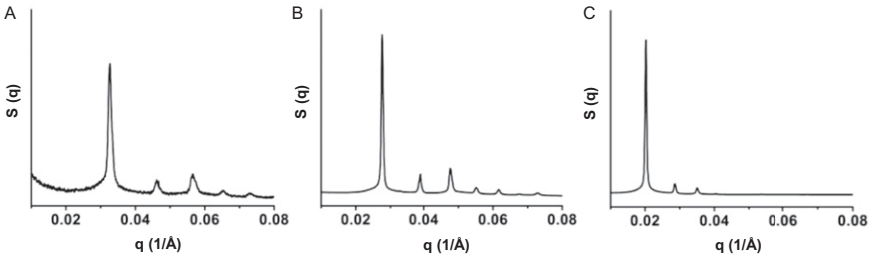

Fig. S1. SAXS data of PPCs. (*A*) Rhombic dodecahedron BCC single crystal with a volume fraction of 0.91% (PPC1) assembled from 5.6-nm gold nanoparticles. (*B*) Rhombic dodecahedron BCC single crystal with a volume fraction of 2.3% (PPC2) assembled from 9.0-nm gold nanoparticles. (*C*) Rhombic dodecahedron BCC single crystal with a volume fraction of 9.8% (PPC3) assembled from 20-nm gold nanoparticles.

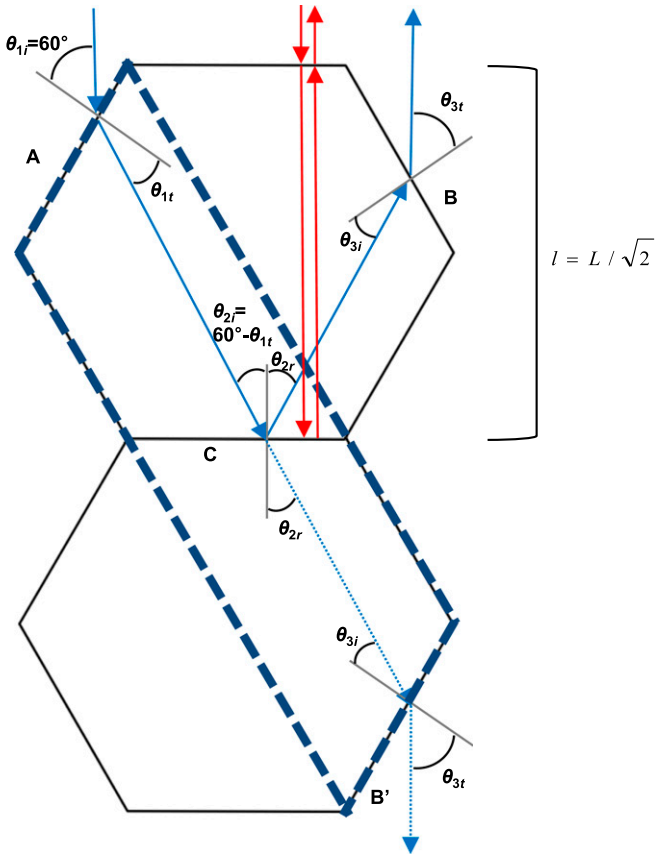

Fig. S2. A geometric optics approximation of scattering channels through the parallel center and side slanted facets for a rhombic dodecahedron dielectric structure. The top hexagon corresponds to that of Fig. 1*B* and the bottom hexagon is a mirror image with respect to the bottom edge of the top hexagon. The parallelogram enclosed with a dashed line shows a geometrical path (**A** to **B**′) equivalent to the actual scattering channel (**A** to **B**). For a light ray incident on **A** to refract through **B**′, a geometric relationship, $\tan^{-1}(1/3\sqrt{3}) < \theta_{1t} < \tan^{-1}(5/3\sqrt{3})$, should be satisfied. θ_{1t} is determined by the refractive indices of the structure and surrounding environment.

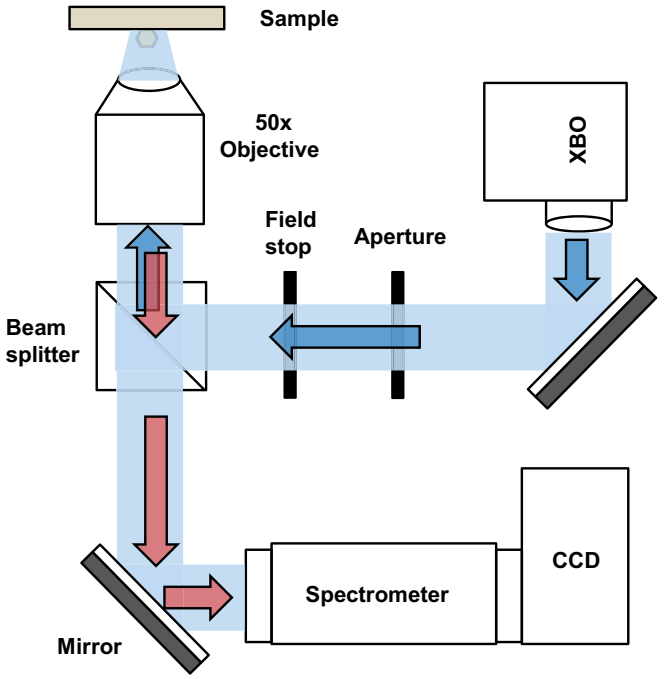

Fig. S3. A schematic description of the backscattering signal detection setup. The blue arrows indicate the light incident on the sample and the red arrows the reflected light. Only the reflection mode, not the transmission mode, is shown.

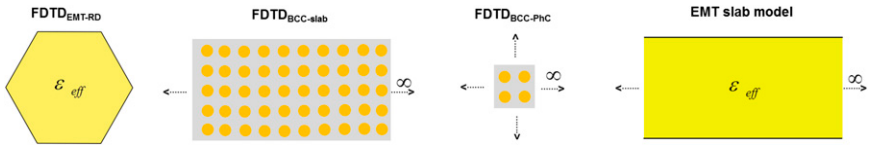

Fig. S4. Three types of FDTD models and one analytical calculation used to predict the light–PPC interaction in this work: FDTD$_{EMT-RD}$, FDTD$_{BCC-slab}$, and FDTD$_{BCC-PhC}$ in section S5 and the infinite slab model based on EMT in section S6. Each 2D scheme presents the geometrical and material configurations in each model.

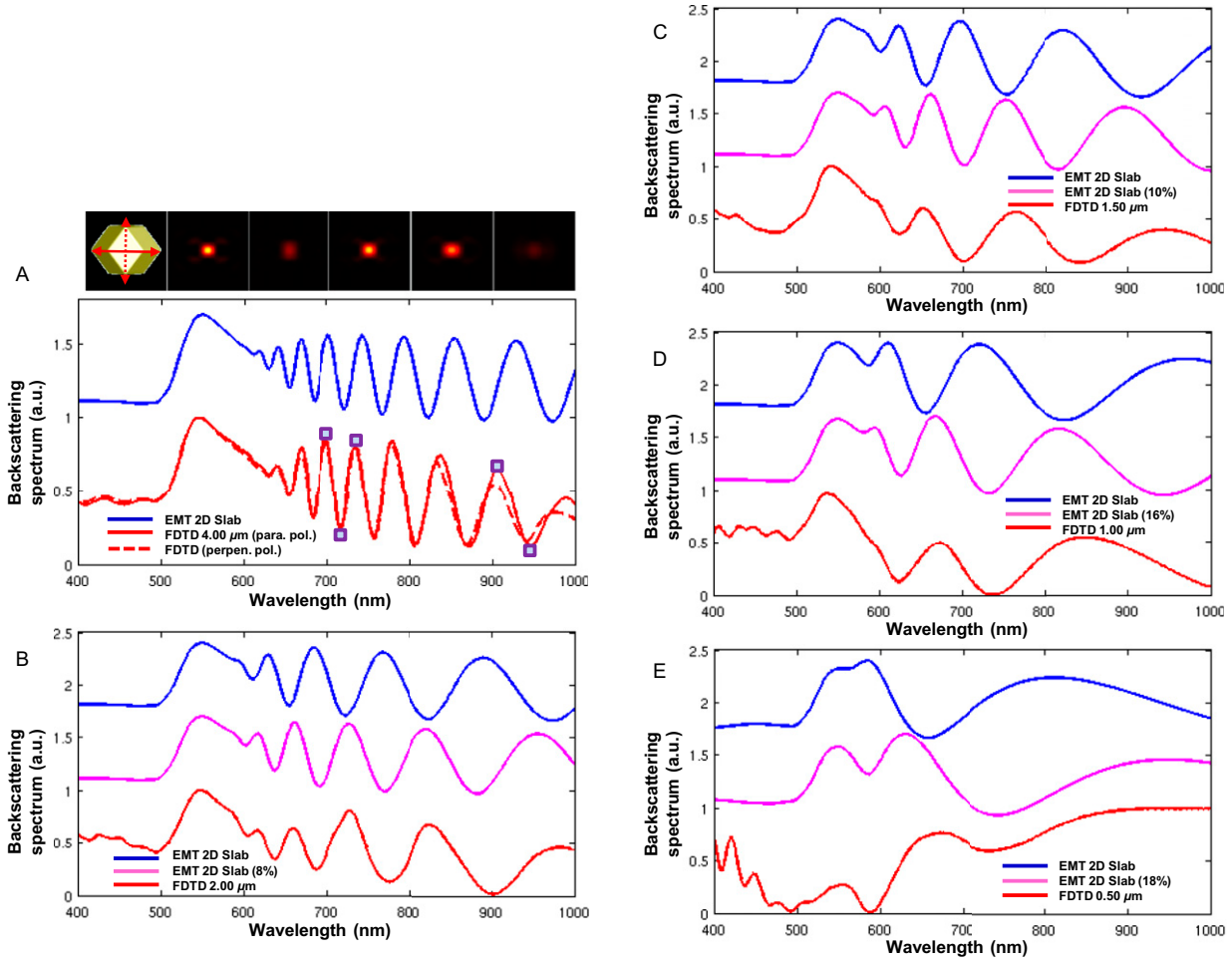

Fig. S5. FDTD-generated FPMs and reproduction of BF image of PPCs. (*A*) The backscattering spectrum from a rhombic dodecahedron with EMT-based refractive index is compared with that of the EMT-based 2D infinite slab model. The volume fraction (*FF*) of gold in the rhombic dodecahedron was 11%. The size of the PPC (*L*) was 4.0 μm and the far-field projection was performed with N.A. 0.8. Two polarization states were used: parallel (red solid line) and perpendicular (red dashed line) to the long axis of the PPC (leftmost figure in the top inset). The top inset shows the far-field projected images at three peaks and two dips in the spectrum for parallel polarization (from left to right, λ = 700.0, 717.4, 734.8, 906.5, and 947.8 nm). The thickness of the slab in the 2D infinite slab model (blue solid line) was 2.828 μm. This corresponds to the distance between the top and bottom facets ($l = L/\sqrt{2}$; Fig. S2). Each spectrum was normalized by its maximum value for comparison. (*B–E*) The same data as in *A* with PPC sizes of 2.0, 1.5, 1.0, and 0.5 μm, not including the perpendicular polarization. The spectra based on the 2D infinite slab model with slightly increased thicknesses (*B*, 8; *C*, 10; *D*, 16; and *E*, 18% increases) were added (magenta solid lines).

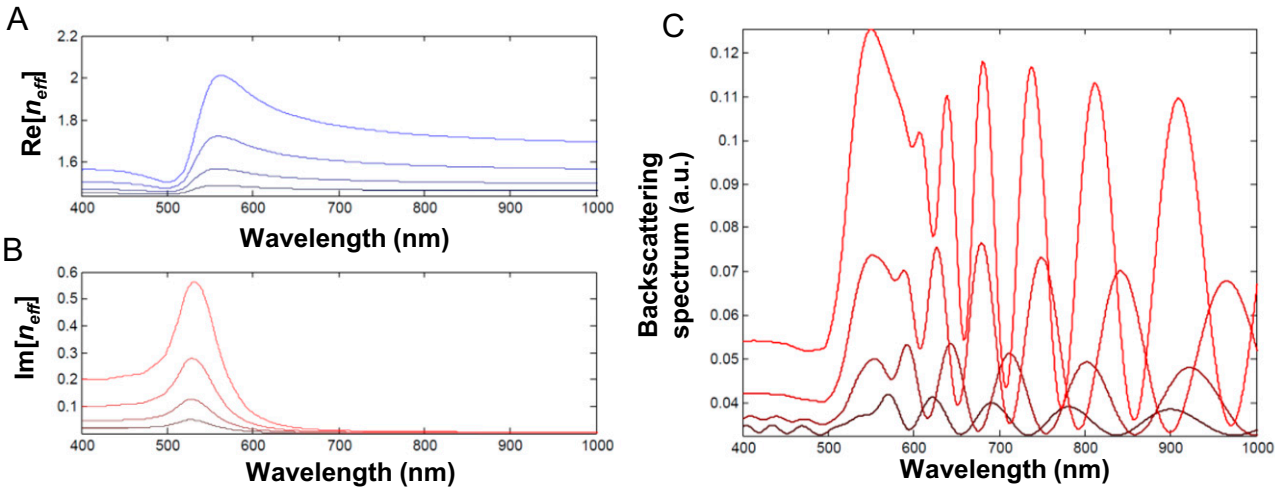

Fig. S6. EMT-generated refractive index and backscattering spectra based on 2D infinite slab model. (*A* and *B*) The real and imaginary parts of PPC effective refractive indices calculated by EMT. The gold volume fractions are *FF* = 0.91 (PPC1), 2.3 (PPC2), and 5.0 and 9.8% (PPC3). The color is bluer (redder) in the real (imaginary) index as *FF* increases. (*C*) Effect of gold particle volume fraction on the reflection spectrum. The slab thickness is 2.0 μm and the same volume fractions are used in *B*. The indices of the surrounding media are n_0 = 1.00 and n_t = 1.44.

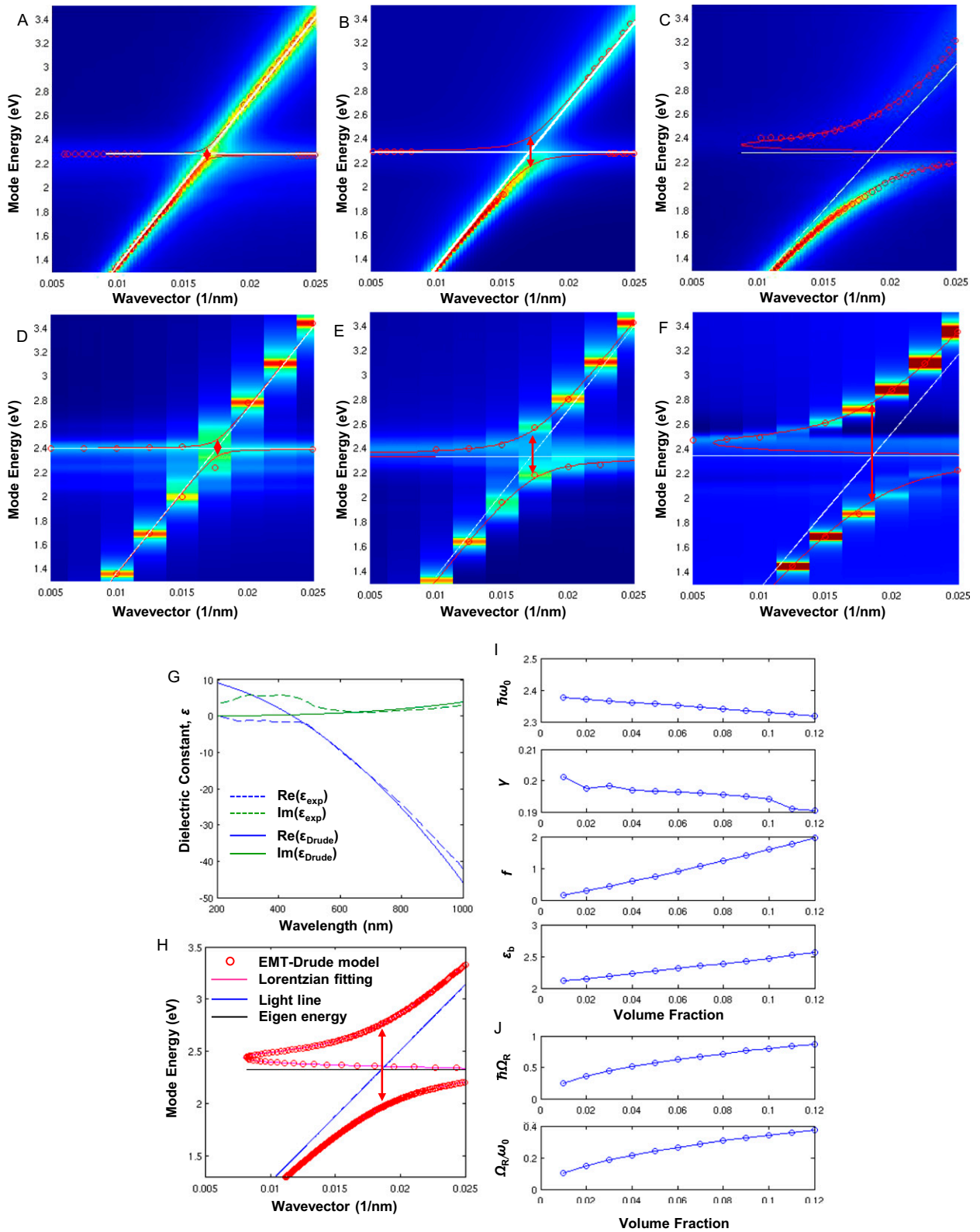

Fig. S7. FDTD and EMT-based dispersion diagrams and their fitting data based on a Lorentzian line shape for PPC1–3. (*A–C*) Dispersion diagrams generated by FDTD photonic crystal analyses with experimentally measured dielectric constant (8). These are identical to Fig. 3 *A–C*, and a larger plot range is used to show fitting data points (circles). The fitted curves are indicated by red solid lines. (*D–F*) The same type of data as in *A–C* with gold dielectric constants generated by a Drude model. The upper bands are visible for PPC3 owing to the absence of the gold interband transition. (*G*) The real and imaginary parts of dielectric constants [experimental (8) and Drude model-based; dashed and solid lines, respectively] used to generate *A–F*. (*H*) An EMT-based dispersion diagram generated with a Drude model for PPC with 10% gold volume fraction. The dispersion curve is fitted with a Lorentzian line shape. (*I*) Four different Lorentzian

Legend continued on following page

fitting parameters, ε_b (background dielectric constant), γ (damping factor), ω_0 (eigen-frequency of polar materials), and f (oscillator strength), generated by fitting the dispersion information as in *H*. (*J*) The mode splitting data based on $\hbar\Omega_R$ and $\hbar\omega_0$ values extracted as in *H* (red arrow and black solid line).

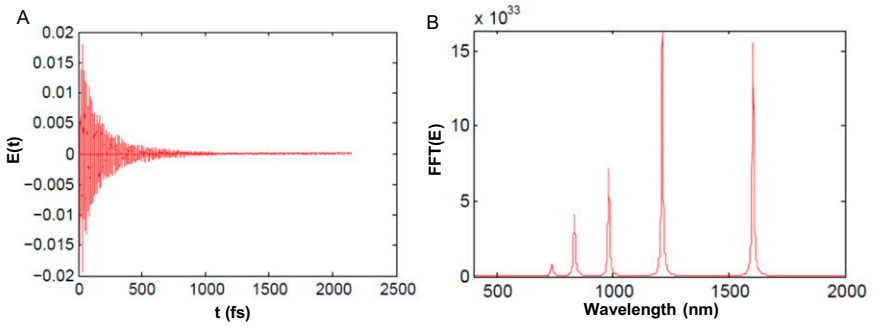

Fig. S8. *Q* Factor calculation. (*A*) Electric field within the BCC crystal in the time domain (femtoseconds) generated by $FDTD_{BCC\text{-}slab}$ for PPC3 with silver coating thickness of 30 nm. (*B*) Frequency domain expression for the electric field in *A* generated by Fourier transform. The peaks indicate FPMs.

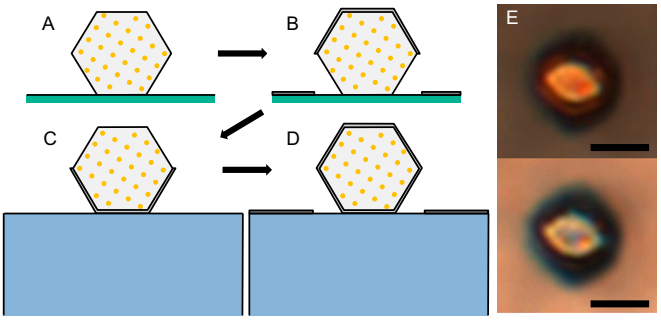

Fig. S9. PPC silver coating process. (*A*) A PPC on a glass slide. (*B*) A silver layer is deposited on the PPC. (*C*) The uncoated bottom side of the PPC is exposed after sticking the PPC to the top surface of a PDMS pillar. (*D*) Another layer of silver is deposited on the uncoated side. (*E*) The top image shows a PPC at step *C* and the bottom step *D*. A 100× objective was used. (Scale bars, 2 μm.)

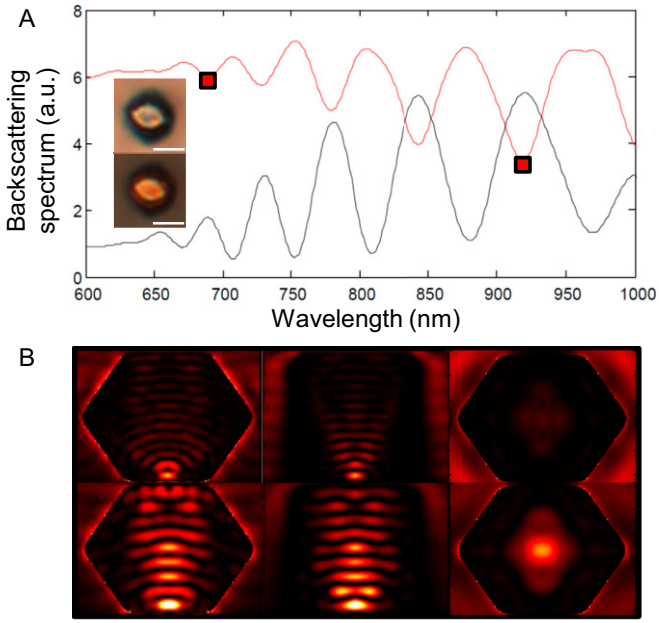

Fig. S10. Backscattering spectra and FPM near-field intensity profiles of a silver-coated PPC3. (*A*) Measured backscattering spectra from the PPC3 before (black) and after (red) the top surface is coated with 30 nm of silver. (*Inset*) Optical images of PPC3 before (*Bottom*) and after (*Top*) the top surface is coated. The colors of the PPC top facet are consistent with the spectral intensity distributions. As expected, the FPMs are not visible below 650 nm (red solid line), even by enhancing FPMs with the silver coating layer owing to the presence of a polariton gap. (Scale bar, 2 μm.) (*B*) Near-field intensity profiles within PPC3 at 684.8 nm (top row) and 927.9 nm (bottom row) (markers in *A*) generated by $FDTD_{EMT\text{-}RD}$ of PPC3. In each row, left and middle images are the vertical cross-sections including the long and short axes in Fig. 1*A*, and the right image is the horizontal cross-section including the long and short axes.

Table S1. DNA sequences used to direct AuNP crystallization

DNA strand name	DNA sequences
For 9.0- and 20-nm samples (PPC2 and PPC3)	
Type A	5′-TAT CGT ATT TAC TCT GAT TTT TTT TTT T-SH-3′
Type B	5′-ACA TCC ACG TAG TCT TAG TTT TTT TTT T-SH-3′
BCC linker A	5′-ATC AGA GTA AAT ACG ATA-A-TTCCTT-3′
BCC linker B	5′-CTA AGA CTA CGT GGA TGT-A-AAGGAA-3′
For 5.6-nm sample (PPC1)	
Type C	5′-TCA ACT ATT CCT ACC TAC (Spacer18)2-SH-3′
Type D	5′-TCC ACT CAT ACT CAG CAA (Spacer18)2-SH-3′
BCC linker C	5′-GTA GGT AGG AAT AGT TGA Spacer18 TTTCCTT-3′
BCC linker D	5′-TTG CTG AGT ATG AGT GGA Spacer18 AAGGAAA-3′

"Spacer18" refers to the spacer Phosphoramidite 18 manufactured by Glen Research.

Table S2. The interparticle distances and lattice parameters for the superlattices

Crystal	Volume fraction, %	$q_{[110]}$, 1/Å	d_{NP}, nm	Lattice constant, nm
Au_20 nm (PPC3)	9.8	0.0202	38.10	43.99
Au_9.0 nm (PPC2)	2.3	0.0276	27.88	32.19
Au_5.6 nm (PPC1)	0.91	0.0327	23.53	27.17